




Research Article

Numerical calculation and finite element analysis for anisotropic elastic properties of carbon fibers: dependence of integration subinterval and mesh size on indentation-derived elastic modulus

Kenta Goto¹ · Kimiyoshi Naito^{2,3}  · Keiichi Shirasu^{2,3} · Ikumu Watanabe²

Received: 10 April 2022 / Accepted: 27 September 2022

Published online: 04 October 2022

© The Author(s) 2022 

Abstract

The elastic modulus measured by indentation of carbon fibers with various anisotropic elasticity is calculated by two numerical approaches, the Vlassak–Nix model and finite element analysis, to reveal the acceptable calculation condition for highly anisotropic materials. Five commercially available carbon fibers that varied in anisotropy index in the range of 0.5–7.9 are used (either polyacrylonitrile- or pitch-based). The numerical error in the calculated modulus increases with the decrease in fiber angle and with the increase in the anisotropy index under the same mesh condition, indicating finer mesh is required for a highly anisotropic material. The acceptable mesh size linearly increases with anisotropic index. The Vlassak–Nix model overestimates the elastic modulus at a small tilt angle if few integration subintervals are used. Conversely, finite element analysis of the Hertz contact problem with coarse mesh underestimates the modulus at a small tilt angle, and a maximum modulus is observed when the fiber is tilted a few degrees against the indentation axis. These findings are expected to assist the future determination of ideal calculation conditions for materials with large anisotropic elasticity including fibers and composites.

Article highlights

- Indentation-derived elastic modulus of highly anisotropic fiber is numerically evaluated.
- The numerical error in the modulus increases with anisotropy index.
- Acceptable resolution that returns accurate modulus are proposed.

Keywords Indentation · Anisotropic elasticity · Vlassak–Nix model · Finite element method · Numerical integration

Supplementary Information The online version contains supplementary material available at <https://doi.org/10.1007/s42452-022-05183-w>.

✉ Kimiyoshi Naito, NAITO.Kimiyoshi@nims.go.jp | ¹National Institute for Materials Science (NIMS), International Center for Young Scientists, 1-2-1 Sengen, Tsukuba 305-0047, Japan. ²National Institute for Materials Science (NIMS), Research Center for Structural Materials, 1-2-1 Sengen, Tsukuba 305-0047, Japan. ³Department of Aerospace Engineering, Tohoku University, 6-6-01, Aza-Aoba, Aramaki, Aoba-ku, Sendai, Miyagi 980-8579, Japan.



SN Applied Sciences

(2022) 4:291

| <https://doi.org/10.1007/s42452-022-05183-w>

SN Applied Sciences
A **SPRINGER NATURE** journal

1 Introduction

Carbon fiber reinforced composites have gained popularity in the fields of aerospace, automotive, and athletic equipment. These composites comprise a lightweight matrix with strong carbon fibers and offer superior specific strength compared to conventional alloys. Consequently, composite materials now account for over half of the body weight of a modern airplane (Boeing 787 and Airbus A350) [1]. The performance of a composite is largely dependent on the mechanical properties of the carbon fibers, which have been investigated by experimental and numerical approaches [2, 3]. Naito et al. characterized the tensile [4], flexural [5], transverse compressive [6], fracture toughness [7], and anisotropy elastic properties [8] of polyacrylonitrile (PAN)- and pitch-based single carbon fibers.

The elasticity of carbon fibers is one of the most fundamental mechanical properties, and is characteristically highly anisotropic with a high stiffness in the longitudinal direction. Transversely isotropic materials, including carbon fibers, have five elastic constants, namely c_{11} , c_{12} , c_{13} , c_{33} , and c_{44} , where direction 3 is parallel to the fiber axis. The small size of the fibers leads to difficulty in elastic constant measurements. Previous studies [9] have calculated these constants of a carbon fiber through ultrasonic measurements of fiber-reinforced composites. An easier measurement method should be developed to assist the evaluation and design of these materials.

Nanoindentation testing can be used to evaluate local mechanical characteristics of microstructures and thin films, including elastoplastic [10], creep [11], and phase transition [12] properties. The technique has been applied to carbon fibers and composites [8, 13]. The indentation test can be used to calculate the reduced elastic modulus (E_r) based on the load–displacement curve at the onset of contact (Hertzian contact condition [14]), as well as the unloading step (Oliver–Pharr method [15]). The indentation-derived elastic modulus (M) is given in Eq. (1):

$$\frac{1}{E_r} = \frac{1 - \nu_i^2}{E_i} + \frac{1}{M}, \tag{1}$$

where E_i and ν_i are the Young’s modulus and Poisson ratio of the indenter, respectively. The M value of an isotropic material is defined according to Eq. (2):

$$M = \frac{E_s}{1 - \nu_s^2}, \tag{2}$$

where subscript s represents the indented sample. The elastic moduli of an anisotropic material are dependent

on crystallographic orientation. Delafargue and Ulm [16] derived closed-form equations for M based on the elastic constants when the longitudinal ($\theta = 0^\circ$) and transverse ($\theta = 90^\circ$) directions of the fibers were used as the indentation axis (M_L and M_T , respectively):

$$M_L = 2 \sqrt{\frac{c_{11} \cdot c_{33} - c_{13}^2}{c_{11}} \left(\frac{1}{c_{44}} + \frac{2}{\sqrt{c_{11}c_{33} + c_{13}^2}} \right)^{-1}}, \tag{3}$$

and

$$M_T = \sqrt{M_L \cdot \frac{c_{11}^2 - c_{12}^2}{\sqrt{c_{11}c_{33}}}}. \tag{4}$$

However, performing an indentation accurately at $\theta = 0^\circ$ on a fiber embedded in a matrix is challenging, which can lead to a large error due to the low M values expected at a tilt angle (θ) below 45° [17].

Vlassak and Nix [18] and Swadener and Pharr [19] proposed theoretical implicit equations for the indentation-derived elastic modulus. In particular, Eqs. (5) to (8) represent the Vlassak–Nix (VN) model:

$$M = 16\pi^2 \left(\int_0^{2\pi} L(\gamma) d\gamma \right)^{-1}, \tag{5}$$

$$L(\gamma) = \alpha_m B_{km}^{-1}(\gamma) \alpha_k, \tag{6}$$

and

$$B_{js}(\mathbf{t}) = \frac{1}{8\pi^2} \int_0^{2\pi} \{ (\mathbf{m}\mathbf{m})_{js} - (\mathbf{m}\mathbf{n})_{jk} (\mathbf{n}\mathbf{n})_{kr}^{-1} (\mathbf{n}\mathbf{m})_{rs} \} d\varphi, \tag{7}$$

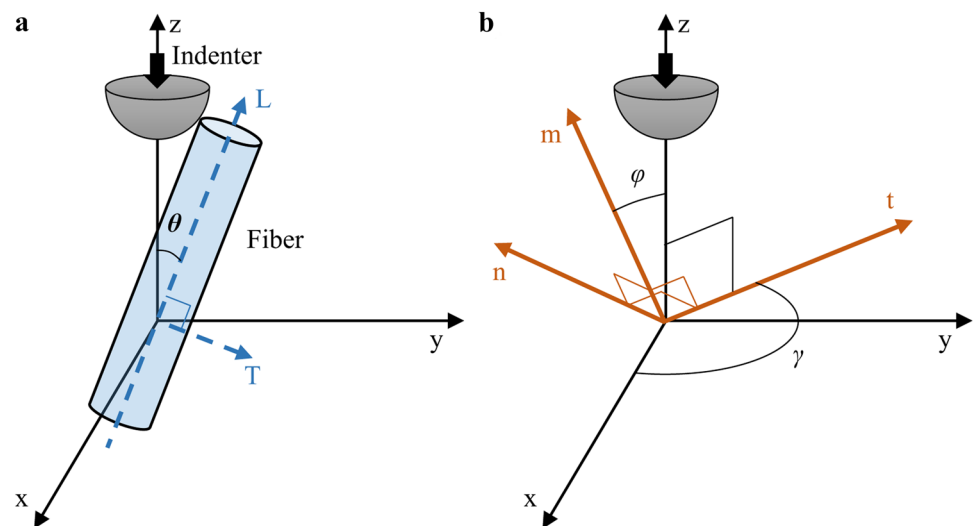
where

$$(\mathbf{a}\mathbf{b})_{jk} = a_i c_{ijkm} b_m. \tag{8}$$

and a represents the direction cosine of the indentation axis toward the fiber coordinate. \mathbf{m} , \mathbf{n} , and \mathbf{t} related to a right-hand Cartesian system, where \mathbf{t} is perpendicular to the indentation axis (Fig. 1). A detailed description of these equations is given in a previous report [18].

Alternatively, M may be calculated using finite element analysis (FEA). The Hertzian contact and indentation of anisotropic single crystals [20, 21] and composite materials [22, 23] have been successfully calculated using FEA. These techniques can be used to calculate M at an arbitrary tilt angle. The accuracy of numerical solutions significantly decreases when an insufficient number of subintervals is used. An example of this is shown during the evaluation of the two integral terms using the VN model (Eqs. (5) to (8)). The subinterval number in FEA corresponds to mesh size,

Fig. 1 Coordinate systems for **a** fiber in blue and **b** VN model in orange (separated for clarity)



which must be verified before the main analysis is conducted. However, few papers elaborate on mesh dependency, although it is the premise of all analyses [24, 25]. Furthermore, fiber materials tend to exhibit more anisotropy than bulk materials, which can cause errors in numerical calculations when anisotropy is not properly considered. The knowledge of the dependence of integration subinterval and mesh size on the indentation-derived elastic modulus helps engineers prepare and verify an analytical model for a carbon fiber with different anisotropy. In addition, it is important to understand the error trends of the indentation-derived elastic modulus of anisotropic materials for the numerical calculations in order to evaluate the confidence of experimental results.

The aim of this study is to investigate the effect of subinterval number and mesh size on the indentation-derived elastic modulus of carbon fibers with high anisotropic elasticity using the VN model and FEA of the Hertzian contact problem. Based on experimental elastic constants of five carbon fibers, the corresponding indentation-derived elastic modulus plots are determined as a function of tilt angle. The indentation-derived elastic moduli of five carbon fibers with different anisotropic indices are calculated using various subinterval numbers and mesh sizes in the

VN model and FEA, respectively. The relationship between numerical error of the indentation-derived elastic modulus and elastic anisotropy is discussed. In the next section, we show the detail information about the materials, VN model and FEA. Section 3 shows the effect of subinterval number and mesh size on the indentation-derived elastic modulus of carbon fibers with high anisotropic elasticity using the VN model and FEA. We also discuss about the results and the relationship between numerical error of the indentation-derived elastic modulus and elastic anisotropy. In Sect. 4, we present the conclusion of the studies and show the advantages of this works.

2 Materials and methods

2.1 Materials

Five commercially available carbon fibers were used, namely T800SC, T700SC, M60JB, K13D, and XN05. The first three fibers were PAN-based carbon fibers (Toray Industries, Inc.), and the remaining two were pitch-based carbon fibers (Mitsubishi Chemical Co. and Nippon Graphite Fiber Co., respectively). The elastic constants of each

Table 1 Elastic constants of carbon fibers

	c_{11}^a [GPa]	c_{12}^a [GPa]	c_{13}^a [GPa]	c_{33}^a [GPa]	c_{44}^a [GPa]	A_L [-]	M_L [GPa]	M_T [GPa]
T800SC	21.6	4.4	5.2	296.1	8.6	2.5	91.9	22.7
T700SC	19.4	4.0	4.7	235.9	8.9	2.2	81.9	20.9
M60JB	13.2	2.7	3.2	589.3	4.7	5.0	100.2	13.8
K13D	4.5	0.9	1.1	935.4	3.6	7.9	110.2	5.7
XN05	27.8	6.2	6.8	56.7	5.8	0.5	32.0	24.3

^aRef. [8]

carbon fiber were calculated using Eqs. (3) to (7) shown in a previous report [17] that was based on Young’s modulus in the longitudinal direction (E_L), Poisson ratios in the transverse–transverse (ν_{TT}) and longitudinal–transverse (ν_{LT}) directions, and the indentation-derived elastic moduli (M_L and M_T). E_L , M_L , and M_T were obtained through tensile and indentation experiments, and ν_{TT} and ν_{LT} were both assumed to be 0.2 [4, 7]. A detailed description of these equations is provided in a previous report [8], where M_L was denoted by M_{L0} . The elastic constants and anisotropy indices (A_L) [26] of the fibers are provided in Table 1, where $A_L=0$ for an isotropic material. The K13D and M60JB fibers were more anisotropic, while XN05 was the most isotropic.

2.2 Methods

The indentation-derived elastic moduli of carbon fibers were calculated using the VN model and FEA, where the tilt angle of the fiber was varied. The calculated elastic constants were used as input parameters in the VN model and FEA. The coordinate system used in this study is shown in Fig. 1, where θ denotes the angle between the indentation and fiber axes (i.e. tilt angle) and ranged

from 0° to 90° . The VN model includes two integral terms (Eqs. (5) and (7)). The midpoint rectangle rule was employed during numerical integration for simplicity and the number of integration subintervals (n_{VN}) varied up to 1000, as shown in Eq. (9):

$$\int_0^{2\pi} f(x)dx \rightarrow \sum_{i=1}^{n_{VN}} \left\{ f\left(\frac{2\pi(i-0.5)}{n_{VN}}\right) \times \frac{2\pi}{n_{VN}} \right\}. \tag{9}$$

We confirmed that our code implementing the VN model based on Eqs. (5) to (8) agreed with the previous report (Supplementary S1) [17], and increments of 1° and 5° were used when θ ranged 0° – 10° and 10° – 90° , respectively.

FEA was conducted for the Hertzian contact problem using a commercial software package (ABAQUS, version 2019). As well as the VN model, it was assumed that the fiber is much larger than the indented area to compare with the calculation result using the VN model, though many carbon fibers have below $10\ \mu\text{m}$ in diameter. The dimensions of the indented component were $35,429\ \mu\text{m} \times 17,715\ \mu\text{m} \times 17,715\ \mu\text{m}$ and the constraints of FEA were shown in Fig. 2. Four finite element models with various mesh sizes were used.

Fig. 2 Finite element models with minimum mesh sizes (l_{FEA}) of **a** 0.9, **b** 0.45, **c** 0.3, **d** 0.15 μm , and **e** constrains

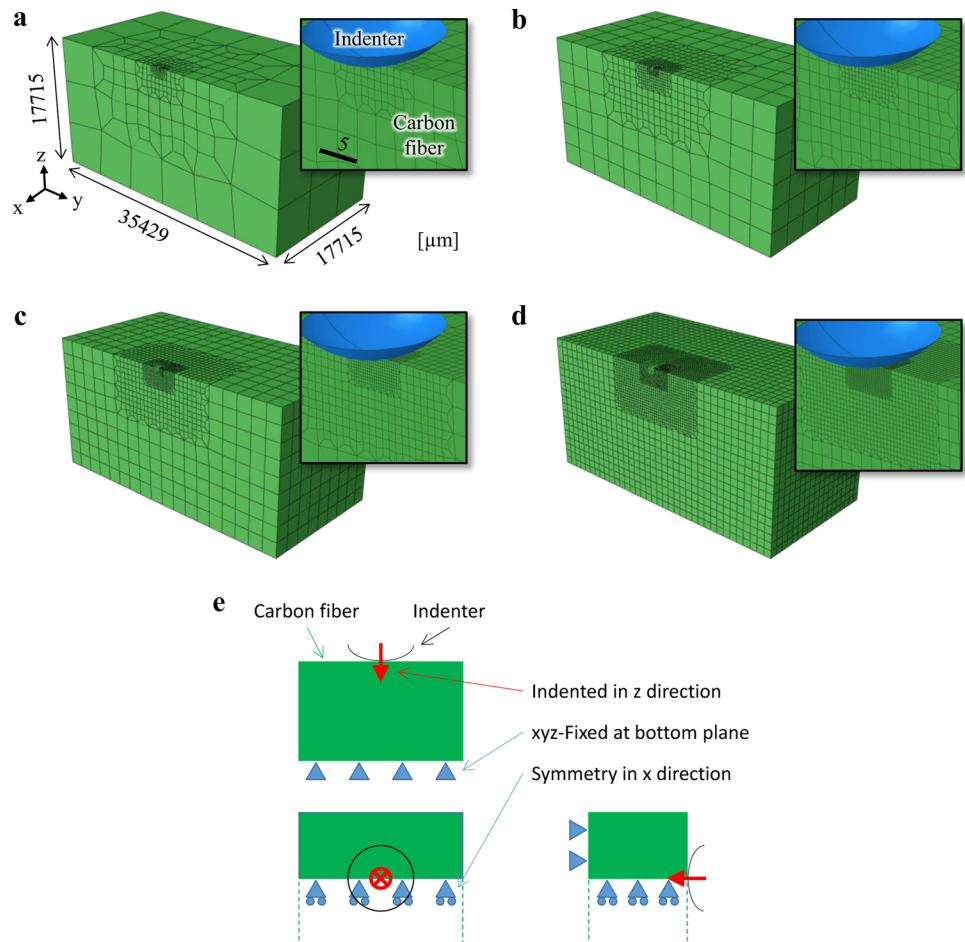


Table 2 Minimum mesh size, nodes, and elements in each finite element model

Model	l_{FEA} [μm]	Number of nodes	Number of elements
A	0.9	1124	908
B	0.45	5201	4540
C	0.3	14,150	12,804
D	0.15	89,189	84,348

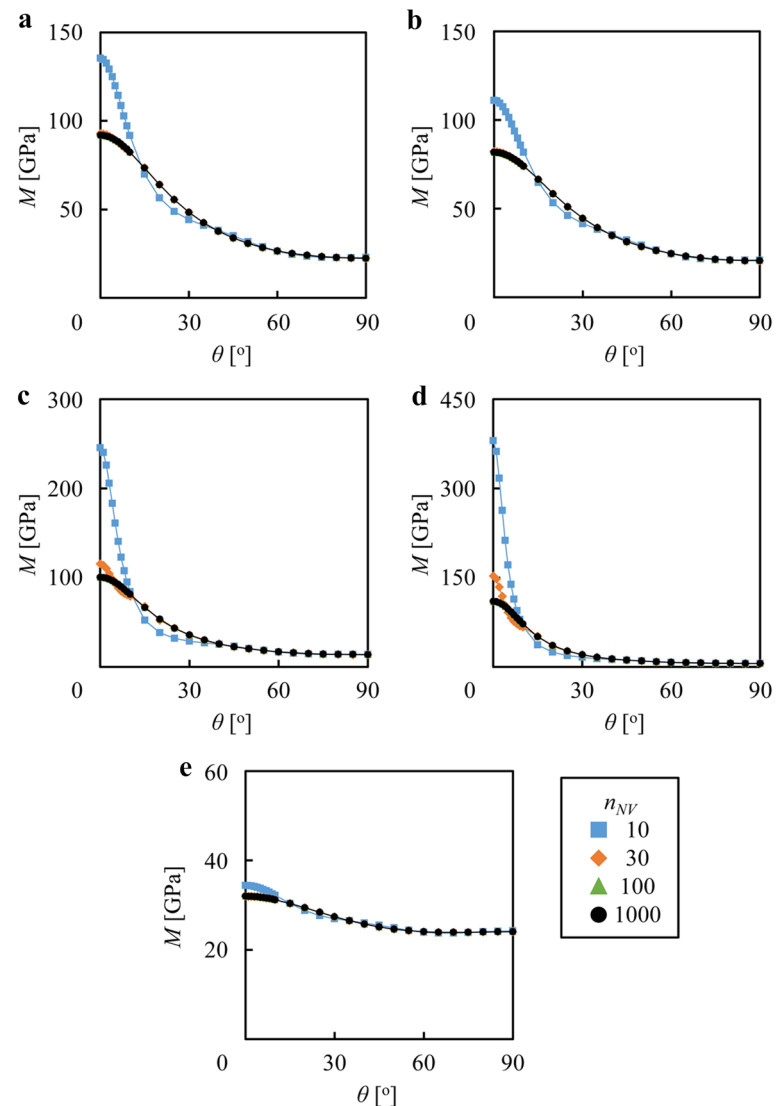
Each model was divided into four regions according to the distance from the indenter, with the element size of each region tripling when going outward as shown in Fig. 2. The minimum element size in each model, l_{FEA} beneath the indenter and number of nodes and elements are given in Table 2. The mirror symmetrical condition was applied at $x=0 \mu\text{m}$, where the fiber direction was rotated around the

x-axis and the bottom face was fixed. The spherical indenter tip had a radius (R) of $10 \mu\text{m}$, and was assumed to be rigid because the indenter was much stiffer than the carbon fibers. The indenter was displaced at $0.05 \mu\text{m}$ in the z-direction for indentation under frictionless contact conditions. The augmented Lagrange method with surface-to-surface discretization was adopted. The indentation-derived elastic modulus was calculated based on the load (P) and displacement (h) of the indenter according to Eq. (10):

$$P = \frac{4}{3} E_r R^{\frac{1}{2}} h^{\frac{3}{2}} = \frac{4}{3} M R^{\frac{1}{2}} h^{\frac{3}{2}}, \quad (10)$$

where $M=E_r$ in the case of the rigid indenter. Increments of 2° and 5° was used when θ ranged 0° – 10° and 10° – 90° , respectively.

Fig. 3 Indentation-derived elastic modulus (M) at various tilt angles (θ) and subinterval numbers (n_{NV}) calculated using the Vlassak–Nix model for commercially available carbon fibers **a** T800SC, **b** T700SC, **c** M60JB, **d** K13D, and **e** XN05



3 Results and discussion

3.1 Subinterval dependency in Vlassak–Nix model

The indentation-derived elastic moduli were calculated for a range of tilt angles at various subinterval numbers using the VN model (Fig. 3). The maximum value of M of all of the fibers was observed at a tilt angle of 0° , and monotonically decreased as the angle increased after a large initial drop. M was not affected when the number of integration subintervals was greater than 100, and the corresponding M values at tilt angles of 0° and 90° agreed well with the M_L and M_T values, respectively, calculated using Eqs. (3) and (4) (Table 1).

The calculated M was higher than the value of $n_{VN} = 1000$ at a tilt angle of 0° and less between 10° and 45° when the subinterval number was too small. The calculation error was larger at the fiber with larger anisotropic index. For example, M at $\theta = 0^\circ$ was 345% higher for the K13D carbon fiber ($A_L = 7.9$), but only 8% higher for XN05 ($A_L = 0.5$) when $n_{VN} = 10$. The integrand defined in Eq. (6), $L(\gamma)$, was plotted against γ at tilt angles of 2° , 4° , and 8° , and is presented as polar graphs in Fig. 4. The indentation-derived elastic modulus was proportional to the reciprocal of the inner area, and the curve adopted an elliptical form when the subinterval number was sufficiently large. The curve of the XN05 carbon fiber (Fig. 4a) exhibited a circular shape, even at a small subinterval number of 10.

However, this was not observed in K13D. Smaller subinterval numbers led to a smaller inner area at a tile angle of 2° (Fig. 4b), thus leading to a high M value. The integrated term increased with increasing tilt angle in the first and third quadrants (Fig. 4c). The plots adopted a peanut shape below 30 subintervals when the tilt angle was 8° (Fig. 4d). Consequently, the inner area was larger than at 1000 subintervals, leading to a lower calculated M value. Thus, the large error at small subinterval numbers was

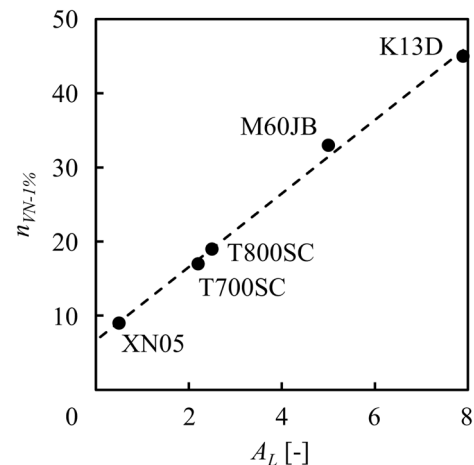
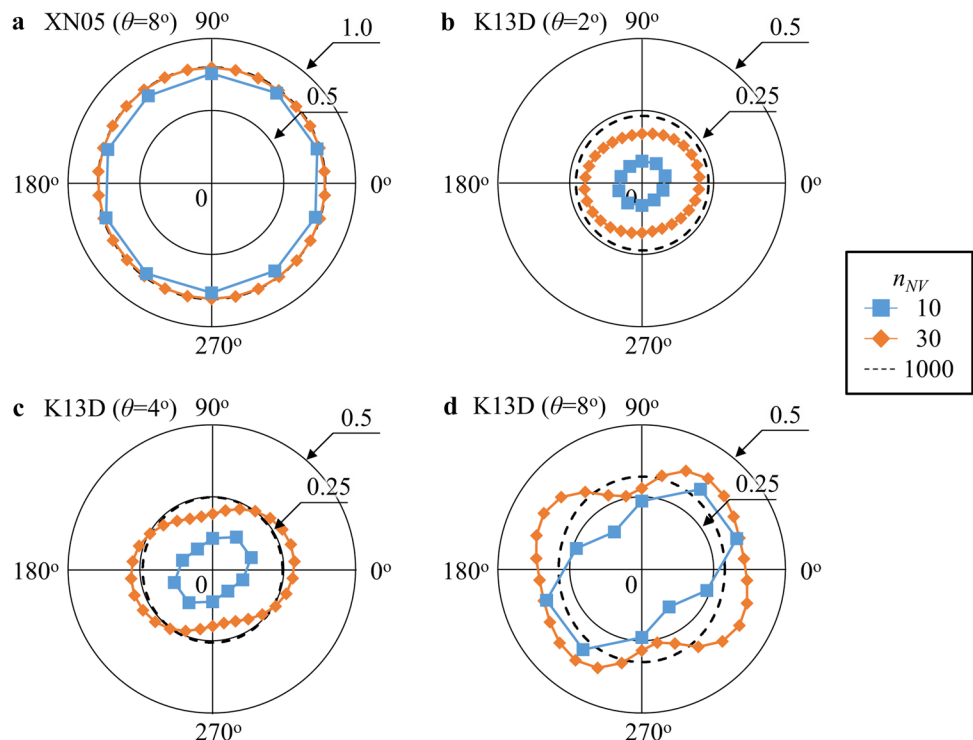


Fig. 5 The anisotropy index (A_L) and minimum subinterval number (n_{VN}) required to achieve an RMS_{VN} error below 1% in various commercially available carbon fibers

Fig. 4 Polar plots of the relationship between $L(\gamma)$ and γ at tilt angles of **a** 8° (XN05 carbon fiber), **b** 2° (K13D carbon fiber), **c** 4° (K13D carbon fiber), and **d** 8° (K13D carbon fiber)



mainly attributed to the decrease in the accuracy of the Green function \mathbf{B} (Eq. (7)).

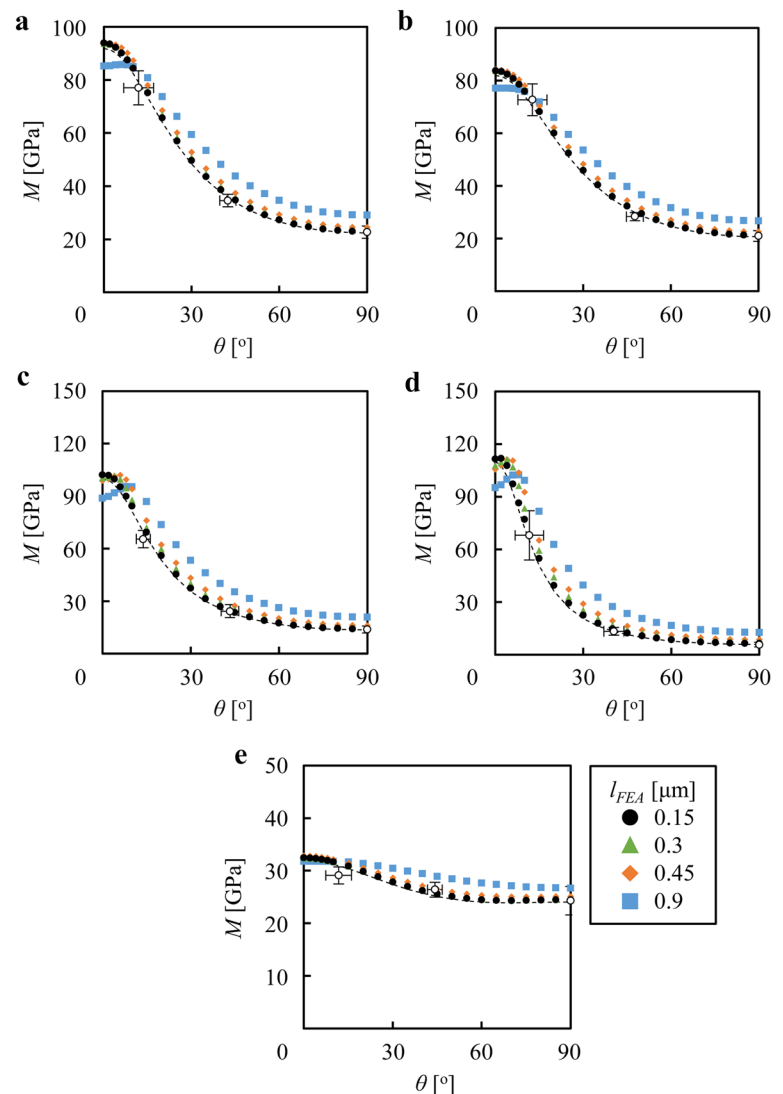
The residual root-mean-square error (RMS_{VN}) of M at each subinterval number was calculated, as shown in Eq. (11):

$$RMS_{VN} = \sqrt{\sum_{\theta} \left(\frac{M_{\theta}(n_{VN}) - M_{\theta}(1000)}{M_{\theta}(1000)} \right)^2}. \quad (11)$$

The minimum subinterval number at which an RMS_{VN} error of less than 1% was achieved ($n_{VN-1\%}$) was plotted against anisotropy index in Fig. 5. The subinterval number required to achieve a small error linearly increased with increasing anisotropy index, where the line of best fit is given in Eq. (12):

$$n_{VN-1\%} = 4.9A_L + 6.7. \quad (12)$$

Fig. 6 Indentation-derived elastic modulus (M) values at various tilt angles (θ) and mesh sizes (l_{FEA}) calculated using finite element analysis for commercially available carbon fibers **a** T800SC, **b** T700SC, **c** M60JB, **d** K13D, and **e** XN05. The dotted lines represent values calculated using the VN model ($n_{VN}=1000$), and open circles show experimental results [8]



Thus, only 10 subintervals were required for an isotropic fiber ($A_L=0$) but over 50 subintervals were used for highly anisotropic fibers ($A_L>8$). The minimum subinterval number was dependent on the integration algorithm, and may be improved using a more sophisticated algorithm than the rectangle rule used in this study (e.g., trapezoidal and Simpson's rules [27]). However, a similar tendency is expected using any algorithm, thus Eq. (12) can still be used to estimate the subinterval number.

3.2 Mesh dependency in finite element analysis

The indentation-derived elastic moduli calculated using FEA exhibited different tendencies than the VN model when the mesh sizes (l_{FEA}) is large, where the relationship between M and tilt angle at various l_{FEA} is illustrated in Fig. 6. The indentation-derived elastic modulus calculated

using the VN model at 1000 subintervals and along with published experimental results [8] are also shown (VN model: dotted line, experimental result: open circle) for comparison. M obtained using FEA and the VN model were similar at smaller mesh sizes. However, the calculated M was lower when the mesh was rough (large l_{FEA}) compared to a fine mesh (small l_{FEA}) at a small tilt angle. Thereafter, a peak M value was observed at a tilt angle of a few degrees. For example, the K13D carbon fiber exhibited an M of 105.7 GPa at $\theta=0^\circ$ when $l_{FEA}=0.45 \mu\text{m}$. The modulus increased slightly as the tilt angle increased, and a maximum value of 111.3 GPa was observed at 4° . It decreased as tilt angle increased further, but was larger than that of $l_{FEA}=0.15 \mu\text{m}$ when a larger mesh size was used.

The distributions of maximum shear stress under the indenter within an isotropic material and the K13D carbon fiber at tilt angles of 0° and 90° were compared in Fig. 7, where $c_{11}=c_{33}$, $c_{12}=c_{13}$, and $c_{44}=(c_{33}-c_{13})/2$ were used as inputs in the simulation of the isotropic material and corresponded to $E_s=935.4 \text{ GPa}$ and $\nu_s=0.00$. The Hertzian contact theory for an isotropic material [14] determined

that the maximum shear stress occurred at $z=0.38a$ when $\nu=0.00$, where a is the contact radius. The calculated indentation-derived elastic moduli of the isotropic material were close to the theoretical values (Fig. 7a). The maximum value for the K13D carbon fiber at a tilt angle of 0° was obtained near the contact surface, and the stress was mainly distributed in the z -direction (Fig. 7b). Thus, the finite element model should sufficiently consider the depth in the z -direction of highly anisotropic samples. The relative error of the calculated M at a tilt angle of 0° changed according to the size of the sample (Fig. 8), as predicted using a two-dimensional axisymmetric model (Supplementary S2). The width (W) and depth (H) of the sample were normalized using $\sqrt{2Rh}$, which approximately corresponded to the contact area. The indentation-derived elastic modulus was underestimated when the model had a high aspect ratio (H/W). When H was small, the modulus was overestimated in the K13D carbon fiber. The stress did not distribute semispherically but anisotropically in the depth direction so that the obtained modulus was affected by the model depth. However, the model with a

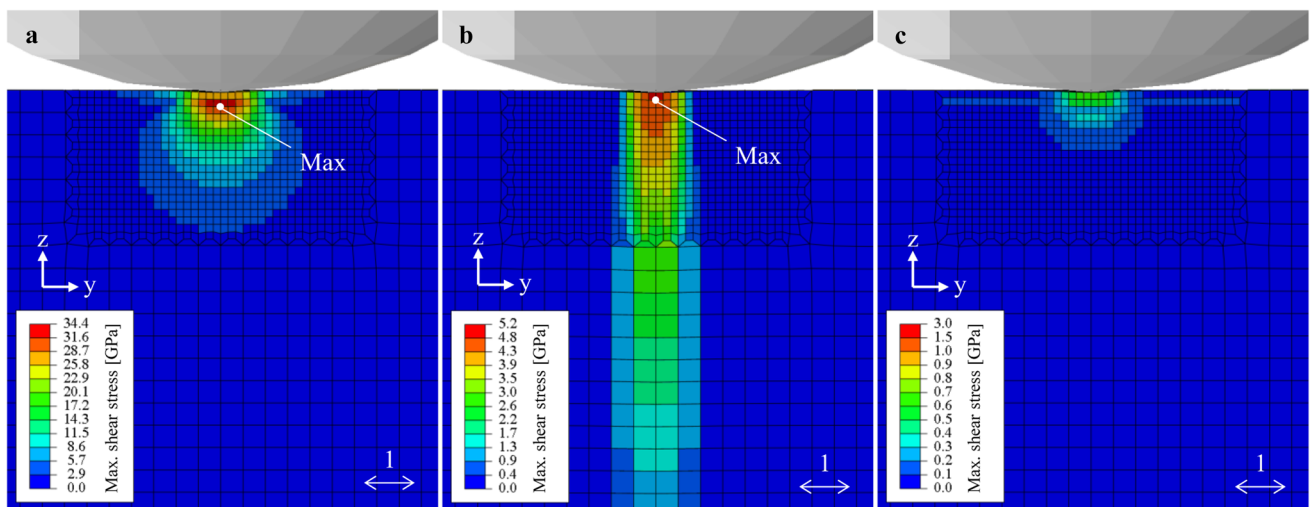
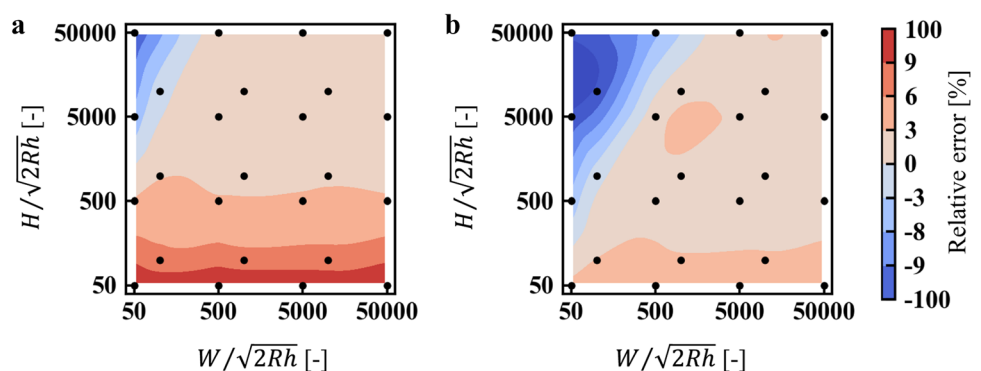


Fig. 7 Distribution of maximum shear stress for **a** an isotropic material, and the K13D carbon fiber at tilt angles of **b** 0° and **c** 90°

Fig. 8 Relative error of the indentation-derived elastic modulus (M) at a tilt angle (θ) of 0° at a normalized height ($H/\sqrt{2Rh}$) and width ($W/\sqrt{2Rh}$) for **a** the K13D carbon fiber and **b** an isotropic material



small H overestimated the modulus for the K13D carbon fiber due to elongation of the stress field in the z -direction. The stress distributed near the K13D carbon fiber surface, particularly that along the fiber direction at a tilt angle of 90° (Fig. 7c), was smaller than that at 0° . Therefore, the

effect of the model width is insignificant if the model has suitable H and H/W .

The models with large l_{FEM} show that M was underestimated at a small tilt angle and overestimated at a large angle. The distributions of displacement (u_z) and normal stress (σ_{zz}) in the z -direction for mesh sizes of 0.15 and

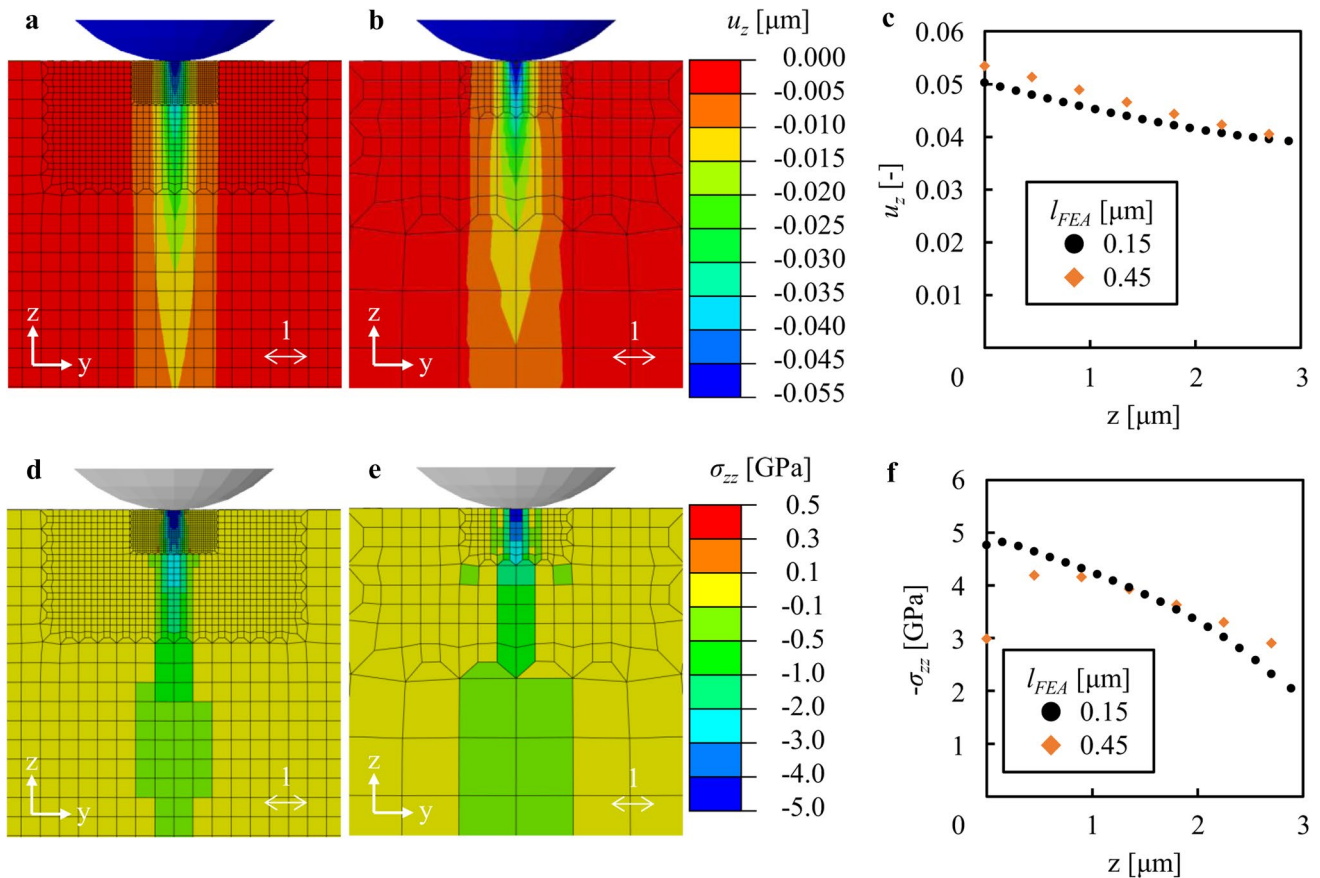
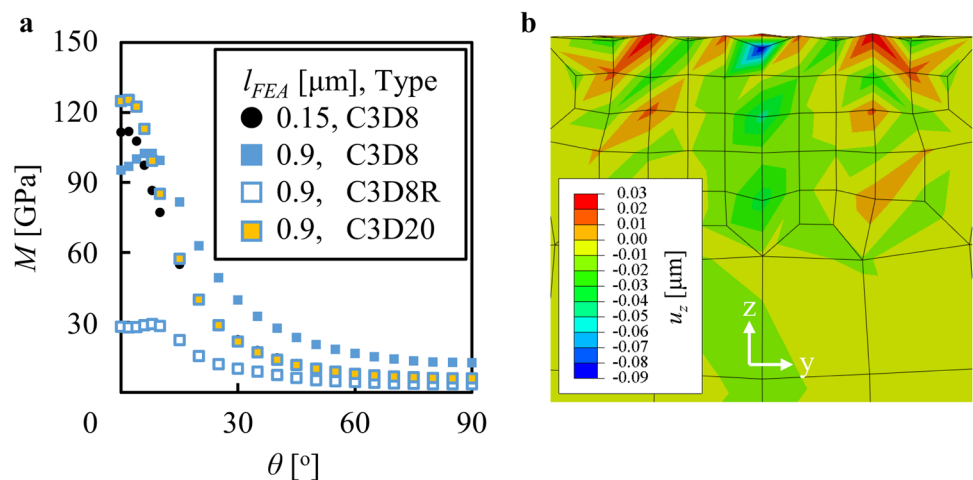


Fig. 9 Distributions of displacements (u_z) and normal stresses (σ_{zz}) at mesh sizes (l_{FEA}) of **a, d** 0.15 μm and **b, e** 0.45 μm at a tilt angle (θ) of 0° and **c, f** plots at $x=y=0$ μm , respectively

Fig. 10 a Indentation-derived elastic modulus (M) at various tilt angles (θ) and element types calculated using finite element analysis for the K13D carbon fiber. **b** Distribution of displacement (u_z) at C3D8R reduced integration element ($l_{FEA}=0.9$ μm and $\theta=0^\circ$), showing hourglass deformation mode



0.45 μm are shown in Fig. 9. The mesh size of 0.45 μm has u_z at $x = y = z = 0 \mu\text{m}$, which is larger than the indentation depth of 0.05 μm because of the contact point extrapolation. The normal stress significantly decreased at the surface, which decreased the indentation load. Thus, M was small at a tilt angle of 0° when a rough mesh was used. The overestimation at a large tilt angle was caused by shear locking. Figure 10a shows a comparison of the element types that were used in the sample. These element types include, first-order full-integration element (C3D8), first-order reduced-integration element (C3D8R), and second-order full-integration element (C3D20). The reduced-integration element, which prevents the shear locking, caused a low modulus because of the hourglass deformation mode, as shown in Fig. 10b [28]. The second-order element returned a high M value at a small tilt angle but showed the same tendency as the C3D8 element model with $l_{FEA} = 0.15 \mu\text{m}$. The present work focused on the simulation with first-order elements, but the second-order element can be used in consideration of time.

The root-mean-square error of the modulus was calculated using the VN model (RMS_{FEA}), as shown in Eq. (13):

$$RMS_{FEA} = \frac{1}{N} \sqrt{\sum_{\theta} \left(\frac{M_{\theta,FEA}(l_{FEA}) - M_{\theta,VN}(n_{VN} = 1000)}{M_{\theta,VN}(n_{VN} = 1000)} \right)^2}, \tag{13}$$

where N denotes the number of FEA calculations for each fiber (= 22). The RMS_{FEA} increased with the anisotropy index (A_L) and mesh size (l_{FEA}), as shown in Fig. 11. The relationship was fitted based on Eq. (14) using the least-squares method:

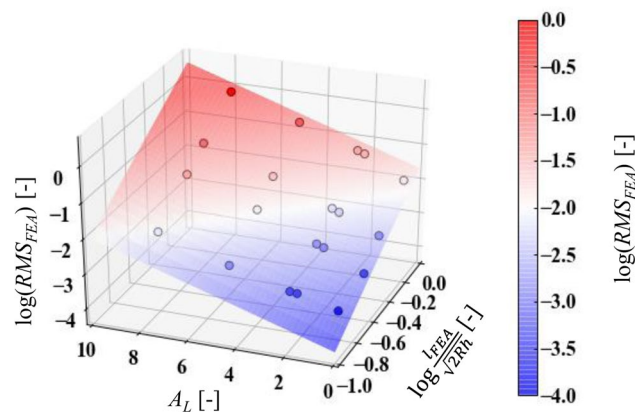


Fig. 11 Root-mean-square (RMS_{FEA}) error of indentation-derived elastic modulus (M) with normalized mesh size ($l_{FEA}/\sqrt{2Rh}$) and anisotropy index (A_L)

$$\ln(RMS_{FEA}) = C_1 \ln\left(\frac{l_{FEA}}{\sqrt{2Rh}}\right) + C_2 A_L + C_3. \tag{14}$$

where $C_1 = 2.5$, $C_2 = 0.49$, and $C_3 = -3.8$. The plane of Eq. (14) is also depicted in Fig. 11. As shown in Eq. (14), the mesh size must be considered to reduce the error of the estimations. For example, mesh sizes should be less than 0.72 μm for an isotropic material and 0.15 μm for the K13D carbon fiber ($A_L = 7.9$) to ensure an RMS_{FEA} value below 0.01.

3.3 Numerical error with respect to experimental results

The numerical error was calculated from the experimental indentation result [8] as shown in Fig. 12, when $n_{VN} = 1000$ for the VN model and $l_{FEA} = 0.15$ for the FEA. The error in all fiber was within $\sim \pm 10\%$, which is comparable to the measurement error. It was the smallest at $\theta = 90^\circ$. Shirasu et al. [8] pointed out θ in the experiment has possible measurement error, especially at small θ due to the measurement technique. The large numerical error at small θ was caused by the measurement error in θ and high sensitivity of M against θ . These findings agree to Castillo and Kalidindi [29], which predicted the variation of M with θ using Monte Carlo Markov Chain and showed highest uncertainty was seen at small θ . Figure 13 shows the dependence of average absolute value of the error on the anisotropy index. The average error was comparable in the VN and FEA results. It was slightly decreased with A_L but almost constant in the VN result, while it increased in the FEA result. Therefore, the VN model is recommended for the calculation of M , especially at high A_L .

These findings can be used to further improve the numerical analysis of anisotropic materials. The range of the anisotropic index of carbon fibers used in this study covers most of the carbon fibers and more attention against the numerical error should be paid when a pitch-based carbon fiber and its composite are calculated.

4 Conclusions

The indentation-derived elastic modulus of the five different carbon fibers with various elastic constants and anisotropic indices ranging from 0.5 to 7.9 were calculated by the VN model and FEA at various tilt angles. The effect of mesh condition in numerical calculations was investigated to minimize the numerical error. The error significantly increased at small subinterval and mesh numbers when the indentation axis was parallel to the fiber longitudinal direction. The carbon fibers with a high anisotropic index

Fig. 12 Numerical errors as a function of tilt angles (θ). **a** T800SC, **b** T700SC, **c** M60JB, **d** K13D, and **e** XN05

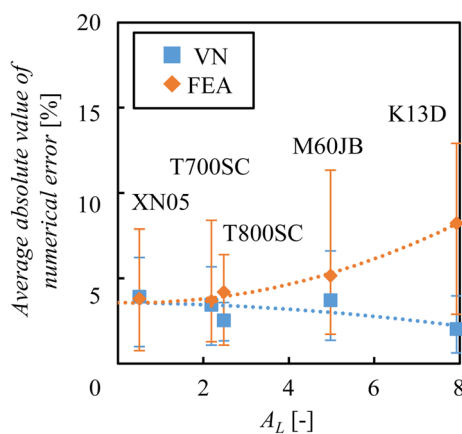
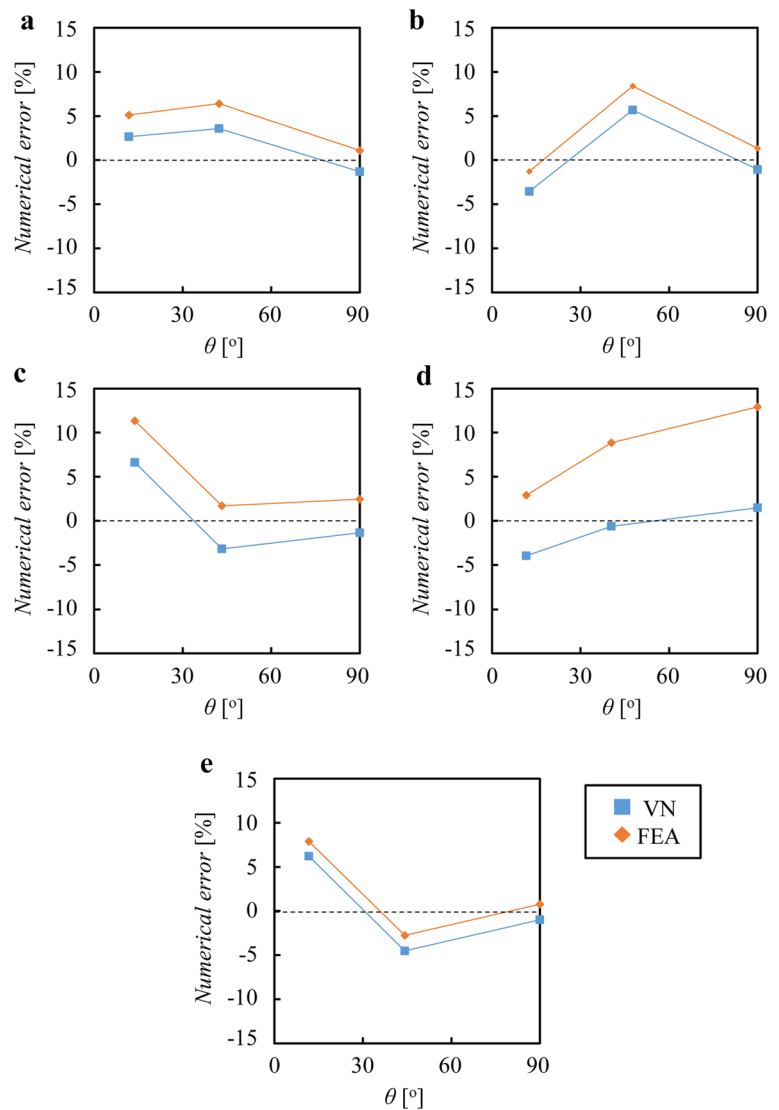


Fig. 13 The average absolute values of numerical errors as a function of anisotropy index (A_L)

were most affected by this phenomenon. The VN model overestimated indentation-derived elastic modulus at a small tilt angle with coarse subintervals due to the integration error of the Green function. However, the FEA underestimated the modulus under the same conditions at a small tilt angle with large l_{FEM} . Carbon fibers with high anisotropy exhibited a maximum indentation-derived elastic modulus at a tilt angle of a few degrees when calculated using FEA. Therefore, it is important to use a larger subinterval number and finer mesh as the anisotropy of the fiber elasticity increases. Furthermore, the finite element models overestimated the highly anisotropic indented samples when an insufficient depth was used. The equations were optimized for the minimum subinterval, mesh size, and finite element model size to minimize calculation errors. The comparison with the experimental indentation-derived elastic modulus showed the numerical error is of less dependence on anisotropic index in the

VN model, but increased in the FEA result, which indicates the VN model is recommended for the calculation of M at high anisotropic index. The convergence of the estimated indentation-derived elastic modulus was strongly dependent on the numerical conditions. For example, the calculation error could be improved when a superior integration algorithm was used in the VN model, or when a high-order mesh type was used in FEA. However, similar tendencies are expected in other numerical conditions. Thus, these findings can be used to further improve the numerical analysis of anisotropic materials. The range of the anisotropic index of carbon fibers used in this study covers most of the carbon fibers. A PAN-based carbon fiber has a relatively small anisotropic index ($A_L < 2$), while a pitch-based carbon fiber shows a large index due to high crystallinity. Therefore, more attention against the numerical error should be paid when a pitch-based carbon fiber and its composite are calculated.

Acknowledgements This research was supported by Council for Science, Technology and Innovation (CSTI), Cross-ministerial Strategic Innovation Promotion Program (SIP), “Materials Integration for revolutionary design system of structural materials” [Funding agency: Japan Science and Technology Agency (JST)].

Author contributions KG: Data curation, Methodology, Visualization, Software, Formal analysis, Investigation, Validation, Writing—Original draft preparation. KN: Conceptualization, Data curation, Methodology, Resources, Supervision, Validation, Writing—Reviewing and Editing. KS: Data curation, Methodology, Visualization, Investigation, Writing—Reviewing and Editing. IW: Conceptualization, Methodology, Resources, Supervision, Validation, Writing—Reviewing and Editing. All the authors read and approved the manuscript.

Funding This research was supported by Japan Science and Technology Agency (JST).

Data availability The datasets supporting the conclusions of this article are included within the article.

Declarations

Conflict of interest The author(s) declared no potential conflicts of interest with respect to the research, authorship and/or publication of this article.

Open Access This article is licensed under a Creative Commons Attribution 4.0 International License, which permits use, sharing, adaptation, distribution and reproduction in any medium or format, as long as you give appropriate credit to the original author(s) and the source, provide a link to the Creative Commons licence, and indicate if changes were made. The images or other third party material in this article are included in the article's Creative Commons licence, unless indicated otherwise in a credit line to the material. If material is not included in the article's Creative Commons licence and your intended use is not permitted by statutory regulation or exceeds the permitted use, you will need to obtain permission directly from the copyright holder. To view a copy of this licence, visit <http://creativecommons.org/licenses/by/4.0/>.

References

1. Pantelakis S (2020) Historical development of aeronautical materials. In: Pantelakis S, Tserpes K (eds) Revolutionizing aircraft materials and processes. Springer, Cham, pp 1–20
2. Wang H, Zhang H, Goto K, Watanabe I, Kitazawa H, Kawai M, Mamiya H, Fujita D (2020) Stress mapping reveals extrinsic toughening of brittle carbon fiber in polymer matrix. *Sci Technol Adv Mater* 21(1):267–277. <https://doi.org/10.1080/14686996.2020.1752114>
3. Guimard JM, Allix O, Pechnik N, Thevenet P (2009) Energetic analysis of fragmentation mechanisms and dynamic delamination modelling in CFRP composites. *Comput Struct* 87(15–16):1022–1032. <https://doi.org/10.1016/j.compstruc.2008.04.021>
4. Naito K, Tanaka Y, Yang JM, Kagawa Y (2008) Tensile properties of ultrahigh strength PAN-based, ultrahigh modulus pitch-based and high ductility pitch-based carbon fibers. *Carbon* 46(2):189–195. <https://doi.org/10.1016/j.carbon.2007.11.001>
5. Naito K, Tanaka Y, Yang JM, Kagawa Y (2009) Flexural properties of PAN- and pitch-based carbon fibers. *J Am Ceram Soc* 92(1):186–192. <https://doi.org/10.1111/j.1551-2916.2008.02868.x>
6. Naito K, Tanaka Y, Yang JM (2017) Transverse compressive properties of polyacrylonitrile (PAN)-based and pitch-based single carbon fibers. *Carbon* 118:168–183. <https://doi.org/10.1016/j.carbon.2017.03.031>
7. Naito K (2018) Stress analysis and fracture toughness of notched polyacrylonitrile (PAN)-based and pitch-based single carbon fibers. *Carbon* 126:346–359. <https://doi.org/10.1016/j.carbon.2017.10.021>
8. Shirasu K, Goto K, Naito K (2020) Microstructure-elastic property relationships in carbon fibers: a nanoindentation study. *Compos B* 200:108342. <https://doi.org/10.1016/j.compositesb.2020.108342>
9. Datta S, Ledbetter H, Kyono T (1989) Graphite-fiber elastic constants: determination from ultrasonic measurements on composite materials. In: Thompson DO, Chimenti DE (eds) Review of progress in quantitative nondestructive evaluation, vol 8. Springer, Boston, pp 1481–1488
10. Eumelen GJAM, Suiker ASJ, Bosco E, Fleck NA (2022) Analytical model for elasto-plastic indentation of a hemispherical surface inclusion. *Int J Mech Sci* 224:107267. <https://doi.org/10.1016/j.jimecs.2022.107267>
11. Ginder R, Nix W, Pharr G (2018) A simple model for indentation creep. *J Mech Phys Solids* 112:552–562. <https://doi.org/10.1016/j.jmps.2018.01.001>
12. Man T, Ohmura T, Tomota Y (2019) Mechanical behavior of individual retained austenite grains in high carbon quenched-tempered steel. *ISIJ Int* 59(3):559–566. <https://doi.org/10.2355/isijinternational.ISIJINT-2018-620>
13. Kanari M, Tanaka K, Baba S, Eto M (1997) Nanoindentation behavior of a two-dimensional carbon-carbon composite for nuclear applications. *Carbon* 35(10–11):1429–1437. [https://doi.org/10.1016/S0008-6223\(97\)00042-0](https://doi.org/10.1016/S0008-6223(97)00042-0)
14. Popov V (2010) Contact mechanics and friction. Springer, Berlin
15. Oliver W, Pharr G (1992) An improved technique for determining hardness and elastic modulus using load and displacement sensing indentation experiments. *J Mater Res* 7(6):1564–1583. <https://doi.org/10.1557/JMR.1992.1564>
16. Delafargue A, Ulm FJ (2004) Explicit approximations of the indentation modulus of elastically orthotropic solids for conical indenters. *Int J Solids Struct* 41:7351–7360. <https://doi.org/10.1016/j.ijsolstr.2004.06.019>

17. Csanádi T, Németh D, Zhang C, Dusza J (2017) Nanoindentation derived elastic constants of carbon fibres and their nanostructural based predictions. *Carbon* 119:314–325. <https://doi.org/10.1016/j.carbon.2017.04.048>
18. Vlassak J, Nix W (1997) Measuring the elastic properties of anisotropic materials by means of indentation experiments. *J Mech Phys Solids* 42(8):1223–1245. [https://doi.org/10.1016/0022-5096\(94\)90033-7](https://doi.org/10.1016/0022-5096(94)90033-7)
19. Swadener J, Pharr G (2001) Indentation of elastically anisotropic half-spaces by cones and parabolae of revolution. *Philos Mag A* 81(2):447–466. <https://doi.org/10.1080/01418610108214314>
20. Dub SN, Haftaoglu C, Kindrachuk VM (2021) Estimate of theoretical shear strength of C60 single crystal by nanoindentation. *J Mater Sci* 56:10905–10914. <https://doi.org/10.1007/s10853-021-05991-2>
21. Nguyen PTN, Abbès F, Lecomte JS, Schuman C, Abbès B (2022) Inverse identification of single-crystal plasticity parameters of HCP zinc from nanoindentation curves and residual topographies. *Nanomaterials* 12(3):300. <https://doi.org/10.3390/nano12030300>
22. Wang H, Zhang H, Tang D, Goto K, Watanabe I, Kitazawa H, Kawai M, Mamiya H, Fujita D (2019) Stress dependence of indentation modulus for carbon fiber in polymer composite. *Sci Technol Adv Mater* 20(1):412–420. <https://doi.org/10.1080/14686996.2019.1600202>
23. Gonabadi H, Oila A, Yadav A, Bull S (2022) Investigation of the effects of environment fatigue on the mechanical properties of GFRP composite constituents using nanoindentation. *Exp Mech* 62:585–602. <https://doi.org/10.1007/s11340-021-00808-4>
24. Leavy R, Brannon R, Strack O (2010) The use of sphere indentation experiments to characterize ceramic damage models. *Int J Appl Ceram Technol* 7(5):606–615. <https://doi.org/10.1111/j.1744-7402.2010.02487.x>
25. Asada T, Ohno N, Tanaka Y (2008) Flat punch indentation analysis of honeycomb structures using implicit homogenization scheme. In: *Advances in heterogeneous material mechanics (ICHMM-2008), Proceedings of the second international conference on heterogeneous material mechanics*. Huangshan, 3–8 June 2008. pp 824–828
26. Kube C (2016) Elastic anisotropy of crystals. *AIP Adv* 6:095209. <https://doi.org/10.1063/1.4962996>
27. Scherer P (2017) *Computational physics*, 3rd edn. Springer, Cham
28. Belytschko T, Ong J, Liu W, Kennedy J (1984) Hourglass control in linear and nonlinear problems. *Comput Methods Appl Mech Eng* 43:251–276. [https://doi.org/10.1016/0045-7825\(84\)90067-7](https://doi.org/10.1016/0045-7825(84)90067-7)
29. Castillo AR, Kalidindi SR (2021) Bayesian estimation of single ply anisotropic elastic constants from spherical indentations on multi-laminate polymer-matrix fiber-reinforced composite samples. *Meccanica* 56:1575–1586. <https://doi.org/10.1007/s11012-020-01154-w>

Publisher's Note Springer Nature remains neutral with regard to jurisdictional claims in published maps and institutional affiliations.